https://doi.org/10.5194/egusphere-2026-2364
Preprint. Discussion started: 20 May 2026


# On the Feasibility of Remotely Sensing the Earth's Magnetic Field Using a Ground-Based Fully Polarimetric Microwave Radiometer

Witali Krochin[1,2], Axel Murk[1,2], and Gunter Stober[1,2]

[1]Institute of Applied Physics, University of Bern, Switzerland
[2]Oeschger Center for Climate Change Research, University of Bern, Switzerland

**Correspondence:** Witali Krochin (witali.krochin@unibe.ch)

**Abstract.** The Zeeman effect affects millimeter-wave emission lines from atmospheric oxygen through the interaction between the molecular magnetic dipole moment and the geomagnetic field, leading to characteristic line splitting and polarization signatures. Depending on the total angular momentum quantum number, the split components may appear as distinct peaks or as effective line broadening when unresolved. These signatures are observable in molecular oxygen emissions from the stratosphere and mesosphere, where pressure broadening is weak compared to the troposphere. The resulting line shape depends on magnetic field strength, viewing geometry, and polarization. The impact of the magnetic field on the line-spectra provides a potential pathway to remotely sense geomagnetic field perturbations. In this study, we examine the feasibility of such measurements using two oxygen fine-structure transitions at 53.067 GHz and 53.596 GHz. Radiative transfer simulations and synthetic retrievals indicate sensitivity to magnetic field perturbations at altitudes between 30 and 75 km. The method is further evaluated using fully polarimetric observations from the Campaign Temperature Radiometer (TEMPERA-C) during a geomagnetic storm associated with a strong solar flare in January 2026. Applying the developed inversion scheme, we retrieve a perturbation of the vertical magnetic field component of -130 $\pm$ 62 nT for the event.

## 1 introduction

The geomagnetic field is routinely monitored using in situ magnetometers at ground observatories, providing extensive spatial coverage of the near-Earth environment. In addition, satellite missions such as CLUSTER (Escoubet et al. (2001)), CHAMP (Reigber et al. (1999)), THEMIS (Angelopoulos (2008)), ØRSTED (Neubert et al. (2001)), SWARM (Friis-Christensen et al. (2008)), and GOES (Vargas (2024)) have enabled high-precision mapping of Earth's magnetosphere, improved our understanding of geomagnetic storms and substorms, and enhanced space-weather forecasting capabilities. Despite these advances, in situ measurements inherently leave a gap in observational coverage between the Earth's surface and typical satellite orbital altitudes. An alternative approach is the remote sensing of the geomagnetic field via passive microwave observations of the Zeeman line splitting. Yee et al. (2017) demonstrated that the Zeeman-split oxygen line at 118.75 GHz, observed by the Microwave Limb Sounder (EOS MLS, Waters et al. (2006)), can be used to estimate magnetic field perturbations near 105 km altitude. This line splits into three Zeeman sublevels (Schwartz et al. (2006)) with a frequency separation that is directly proportional to the local magnetic field strength, enabling retrieval of line-of-sight (LOS)–averaged magnetic field perturbations. An improved

https://doi.org/10.5194/egusphere-2026-2364
Preprint. Discussion started: 20 May 2026


retrieval framework was later presented in Yee et al. (2021), incorporating polarization effects to determine the orientation of the magnetic field relative to the LOS. The Electrojet Zeeman Imaging Explorer (EZIE) mission was developed to exploit this technique for space-based measurements of ionospheric electrical currents (Padmanabhan et al. (2022); Misra et al. (2022, 2025)) and was successfully launched in 2025. The use of the Zeeman 118.75 GHz line splitting to infer magnetic field variations was previously mentioned by Larsson et al. (2013), who simulated Zeeman observations in the Martian atmosphere. For ground-based applications, the 118.75 GHz line is not suitable due to the high tropospheric optical depth that prevents detection of the Zeeman substructure from the surface. An alternative candidate is the 233.95 GHz transition of the $^{16}O^{18}O$ isotopologue, which contains six Zeeman components and remains observable with ground-based microwave radiometers (Pardo et al. (1995); Johansson et al. (2025)).

In this manuscript, retrievals of the geomagnetic field from ground-based observations of oxygen fine structure lines around 53 GHz are discussed. These lines are commonly used for temperature sounding and are typically split into over 100 Zeeman sublevels. To investigate the sensitivity to the magnetic field, we analyze radiative transfer simulations and perform synthetic retrievals using simulated line spectra. We also outline in detail the influence of the observation geometry and instrument polarization. The analysis shows the potential for retrieving the vertical component of Earth's magnetic field in the range from 35-70 km with a vertical resolution of 10-15 km, provided that the azimuth (az) and elevation (el) angles are optimally chosen to ensure a maximal measurement response. We use the developed inversion algorithm to retrieve the vertical field component from observations made with a ground-based fully polarimetric radiometer at 53 GHz (Krochin et al., 2022, 2026). Although the instrument is not designed to meet the sensitivity requirements indicated by the simulations, a signature in the field perturbation of -130 $\pm$ 62 nT was detected during a geomagnetic storm in January 2026. This finding demonstrates a response to the magnetic field in the observed spectra and promises a pathway towards continuous, ground-based remote sensing of geomagnetic field variations.

## 2 Theory

### 2.1 Stokes Formalism

The Stokes vector is a four-component vector that represents the full polarization state of an electromagnetic field. In the orthogonal basis of the vertically and horizontally polarized electric field components $E_v, E_h$, the four Stokes parameters are defined as:

$$I = \frac{1}{\eta}\left(\left\langle |E_v|^2 \right\rangle + \left\langle |E_h|^2 \right\rangle\right), \tag{1}$$

$$Q = \frac{1}{\eta}\left(\left\langle |E_v|^2 \right\rangle - \left\langle |E_h|^2 \right\rangle\right), \tag{2}$$

$$U = \frac{2}{\eta}\Re\{\langle E_v E_h^* \rangle\}, \tag{3}$$

$$V = \frac{2}{\eta}\Im\{\langle E_v E_h^* \rangle\}. \tag{4}$$

https://doi.org/10.5194/egusphere-2026-2364
Preprint. Discussion started: 20 May 2026


Where $\eta$ is the wave impedance of the medium and $\langle ... \rangle$ denotes cross correlation. For many applications, the modified Stokes parameters are more suitable:

$$S_v = \frac{1}{2}(I+Q), \tag{5}$$

$$S_h = \frac{1}{2}(I-Q), \tag{6}$$

$$S_3 = U, \tag{7}$$

$$S_4 = V. \tag{8}$$

In this manuscript, we use the representation of the Stokes vector $\boldsymbol{T_B}$ and modified Stokes vector $\boldsymbol{T_{B,mod}}$ in units of brightness temperature (Randa et al. (2008)):

$$\boldsymbol{T_B} = \begin{bmatrix} T_I \\ T_Q \\ T_U \\ T_V \end{bmatrix} = \frac{\lambda^2}{k_b} \begin{bmatrix} I \\ Q \\ U \\ V \end{bmatrix}, \quad \boldsymbol{T_{B,mod}} = \begin{bmatrix} T_v \\ T_h \\ T_3 \\ T_4 \end{bmatrix} = \begin{bmatrix} T_v \\ T_h \\ T_{45} - T_{-45} \\ T_{lc} - T_{rc} \end{bmatrix} = \frac{\lambda^2}{k_b} \begin{bmatrix} S_v \\ S_h \\ S_3 \\ S_4 \end{bmatrix} \tag{9}$$

Here, $\lambda$ is the wavelength, $k_b$ is the Boltzmann constant. The third and fourth Stokes parameters $T_3, T_4$, are equivalent to the $U$- and $V$- Stokes parameters $T_U$ and $T_V$. The $U$-Stokes represents the difference between the 45° and -45° polarized fields $T_{45}, T_{-45}$, and the $V$-stokes between the right-hand and left-hand circularly polarized fields $T_{lc}, T_{rc}$, respectively.

Furthermore, the reference axes for vertical and horizontal polarization are defined within a local frame, as, for instance, described in Mishchenko et al. (2002). The Cartesian coordinate system is constructed using local geodetic coordinates, where the z-axis represents the altitude, the x-axis is directed along the longitude, and the y-axis along the latitude. The observation direction, denoted as $\hat{n}$, is expressed in polar coordinates using the azimuth $\phi$ and zenith $\theta$ angle. In this frame, the electric field component of vertical polarization, $E_v$, lies in the plane formed by $\hat{n}$ and $\hat{\theta}$ (see Fig. 1), while the horizontal polarization component, $E_h$, lies in the plane defined by $\hat{n}$ and $\hat{\phi}$. This definition is generally unambiguous, except when $\hat{n}$ is aligned with the z-axis. To prevent confusion in this scenario, it is standard practice to also provide an azimuth angle. Although the azimuth is redundant when the viewing direction is directed along the z-axis, it is necessary for defining the polarization planes. Therefore, the azimuth angle will also be specified for simulations and observations in a zenith view where it is relevant. In comparison to this local frame, the instrument's polarization axis is typically rotated by an angle $-\alpha$, which is determined by the properties of the instrument's optics. To transform the observed Stokes vector $\boldsymbol{T_B}$ into the local frame, the polarization plane must be rotated by the angle $\alpha$ around the $\hat{n}$ axis, which is accomplished using the Mueller matrix $\boldsymbol{\Phi}(\alpha)$:

$$\boldsymbol{T_B}' = \boldsymbol{\Phi}(\alpha)\boldsymbol{T_B}, \tag{10}$$

https://doi.org/10.5194/egusphere-2026-2364
Preprint. Discussion started: 20 May 2026


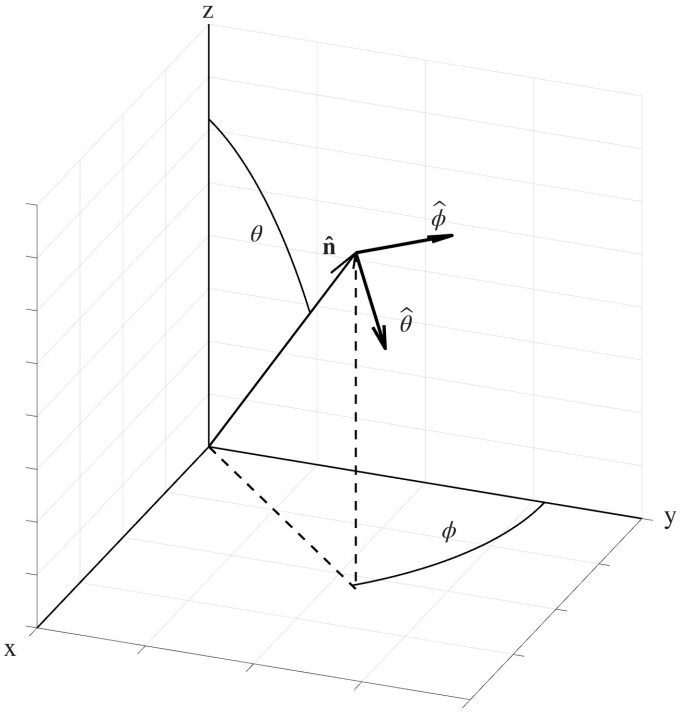


**Figure 1.** Illustration of the local polarization frame. The observation direction $\hat{n}$ is determined by the azimuth $\phi$ and zenith angle $\theta$. The vertical polarization field $E_v$ oscillates in the plane defined by $\hat{n}$ and $\hat{\theta}$, the horizontal polarization field $E_h$ in the plane defined by $\hat{n}$ and $\hat{\phi}$.

where the corresponding Mueller matrix is given in the following form:

$$\mathbf{\Phi}(\alpha) = \begin{pmatrix} 1 & 0 & 0 & 0 \\ 0 & \cos(2\alpha) & \sin(2\alpha) & 0 \\ 0 & -\sin(2\alpha) & \cos(2\alpha) & 0 \\ 0 & 0 & 0 & 1 \end{pmatrix}. \tag{11}$$

### 2.2 Zeeman Effect

The Zeeman effect in the oxygen molecule (Gautier (1967); Lenoir (1967, 1968); Liebe (1981); Rosenkranz and Staelin (1988)) is caused by its total spin state S=1, which results from two unpaired electrons in the electronic ground state and leads to a net magnetic dipole moment. For the rotational angular momentum quantum number N, and total angular momentum quantum number J, fine structure transitions occur within the spin triplet $J = \{N-1, N, N+1\}$. The selection rules for these transitions are $\Delta J = \pm 1$ and $\Delta N = 0$. This restriction allows only two series of transitions: $J \rightarrow J' = N+1 \rightarrow N$, which are usually

https://doi.org/10.5194/egusphere-2026-2364
Preprint. Discussion started: 20 May 2026


denoted as $N^+$, and $J \to J' = N \to N-1$, denoted as $N^-$. Without considering the Zeeman effect the absorption coefficient $\alpha_{J,N,J',N'}$ for a single line is usually calculated by:

$$\alpha_{J,N,J',N'}(\nu) = nS_{J,N,J',N'}F(\nu) \tag{12}$$

Here, $n$ represents the molecular number density of the oxygen molecule, $S_{J,N,J',N'}$ is the line strength for the corresponding transition, $\nu$ is the frequency, and $F(\nu)$ is a lineshape function, typically modeled using the Voigt or Van Vleck-Weisskopf function. In the presence of a magnetic field $\boldsymbol{H}$, one energy level $J$ splits into $2J+1$ energy levels with quantum numbers $M = -J, -J+1, ..., 0, ...J-1, J$. Here, $M$ represents the projection of $J$ on the magnetic field lines. The allowed Zeeman substructure transitions include the $\pi$ transitions with $\Delta M = 0$ and the $\sigma^{\pm}$ transitions with $\Delta M = \pm 1$. The energy distortion due to the magnetic field is:

$$\Delta E = -g\mu_b M \left|\boldsymbol{H}\right|. \tag{13}$$

Where $\mu_b$ is the Bohr magneton and $g$ is the Landé Factor. Consequently the frequency shift $\nu$ for a transition $M \to M'$ is given by:

$$\Delta\nu = \frac{\mu_b \left|\boldsymbol{H}\right|}{h}\left(gM - g'M'\right), \tag{14}$$

where $h$ is the Planck constant. The resulting Zeeman broadened lineshape results from a superposition of line functions from all Zeeman sublevels. Additionally, photons emitted by these transitions exhibit a characteristic polarization pattern that strongly depends on the direction of emission. In a fully polarimetric treatment of the Zeeman effect, the absorption coefficient must be determined for each state of polarization and propagation direction. Therefore, the correspondent coefficient for $\alpha_{J,N,J',N'}(\nu)$ becomes a matrix, known as the propagation matrix $\boldsymbol{\mathcal{K}}_{J,N,J',N'}(\nu)$:

$$\boldsymbol{\mathcal{K}}_{J,N,J',N'}(\nu) = nS_{J,N,J',N'} \sum_{M,\Delta M} S_{M,M'}F(\nu, \nu_0 + \Delta\nu)\boldsymbol{\Phi}_{M,M'} \tag{15}$$

Here, $S_{M,M'}$ is the relative line strength of the Zeeman sublevels, $F(\nu, \nu_0 + \Delta\nu)$ is a normalized Faddeeva line function, and $\nu_0$ denotes the line center of the unsplit line. The term $\boldsymbol{\Phi}_{M,M'}$ represents the Mueller matrix that describes how the radiation is polarized for the corresponding transition and propagation. Qualitatively, the effect of the Mueller matrix can be described as follows: When viewed at a 90° to the magnetic field lines, all components $\pi, \sigma^{\pm}$ will be observed with a linear polarization. Photons from $\pi$ transitions are polarized perpendicularly to the magnetic field lines, while those from $\sigma^{\pm}$ transitions are polarized parallel to the field lines. In contrast, when the viewing direction aligns with the field lines, the $\sigma^{\pm}$ components are circularly polarized while radiation from $\pi$ transitions has zero intensity. In between, $\sigma^{\pm}$ components are polarized elliptically. An illustration of this concept is given in Fig. 2. Apart from this polarization pattern, the Zeeman broadened lineshape for a given observation angle is primarily determined by the frequency offset $\Delta\nu$ and the relative line strength $S_{M,M'}$. The Illustration in Fig. 3 demonstrates how the characteristic shapes of the Stokes parameters relate to the corresponding line strength function. The spectrum of the Q-Stokes shows 3 peaks, one at the center frequency, which

https://doi.org/10.5194/egusphere-2026-2364
Preprint. Discussion started: 20 May 2026


corresponds to the maximal line strength of the $\pi$ components, and two additional peaks outside, which correspond to $\sigma^{\pm}$. The V Stokes spectrum shows two peaks at $\pm 1.12$ MHz from the center, corresponding to the maximal line strength of the circularly polarized $\sigma^{\pm}$ components.

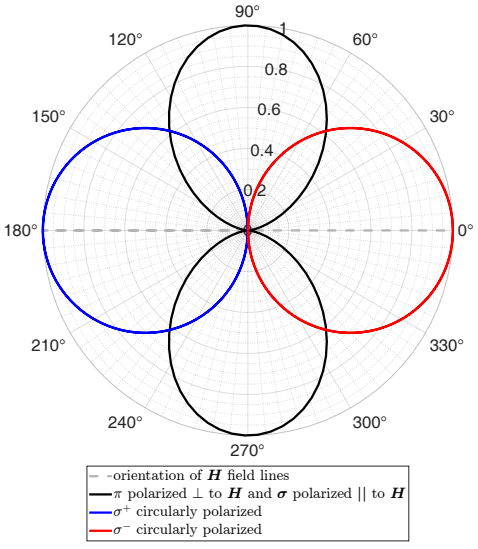


**Figure 2.** Normalized components of the Mueller matrix $\mathbf{\Phi}$ for the individual $\pi$ and $\sigma^{\pm}$ components with the denoted polarization are illustrated in polar coordinates. The angular coordinate represents the angle between LOS and the magnetic field lines.

### 2.3 Inversion Algorithm and Retrieval Quantities

The radiative transfer simulations and inversion algorithms presented in this manuscript are implemented using the Atmospheric Radiative Transfer Simulator version 2.6.18 (ARTS, Buehler et al. (2005), Eriksson et al. (2011), Buehler et al. (2018),Buehler et al. (2024)), along with a Python interface. The calculations of the Zeeman split absorption coefficients, as described in Sec. 2.2, are implemented in ARTS and were discussed in detail in Larsson et al. (2014, 2019).

The optimal estimation algorithm in ARTS uses the mathematical formalism from Rodgers (2000). In this framework, radiative transfer calculations are represented by the forward model $\boldsymbol{F}$, which maps an atmospheric state $\boldsymbol{x}$ on a spectrum $\boldsymbol{y}$ with an additional measurement error $\boldsymbol{\epsilon}$ and forward model parameters $\boldsymbol{b}$:

$$\boldsymbol{y} = \boldsymbol{F}(\boldsymbol{x}, \boldsymbol{b}) + \boldsymbol{\epsilon}. \tag{16}$$

Both the state vector $\boldsymbol{x}$ and the measurement vector $\boldsymbol{y}$ are assumed to be normally distributed relative to a mean atmospheric state. Using Bayesian analysis, the inversion problem is formulated such that the retrieved state $\hat{\boldsymbol{x}}$ represents the atmospheric state with the highest probability for a known forward model spectrum $\boldsymbol{y}$. Under this assumption, the cost function $\boldsymbol{J}$ takes the

https://doi.org/10.5194/egusphere-2026-2364
Preprint. Discussion started: 20 May 2026


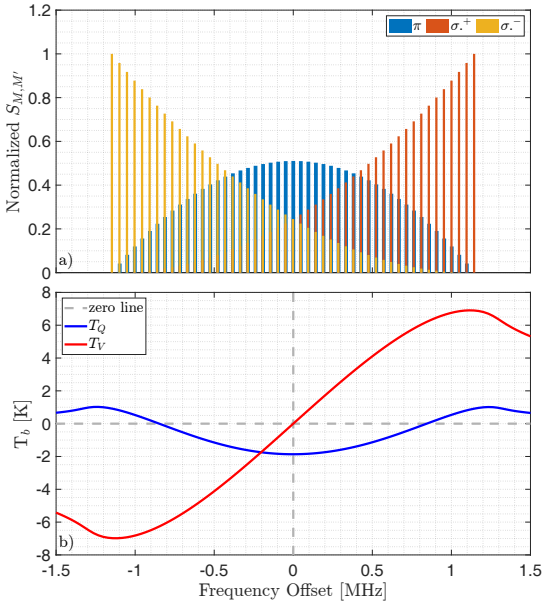


**Figure 3.**

a) Normalized line Strength $S_{J,N,J',N'}$ illustrated as a function of $\Delta\nu$ (Eq. 14). The line strength was calculated for the line with center frequency at 53.596 GHz corresponding to the $25^-$ transition, with a magnetic field magnitude of 41$\mu$T. The Landé factors and line strength function used to generate the plot are discussed in Appendix A.

b) The $T_Q$ and $T_V$ Stokes parameters simulated for a ground-based receiver reflect the structure of the line strength function. Details regarding the radiative transfer simulations can be found in Sec. 4.1.

following form:

$$J(\boldsymbol{x}) = [\boldsymbol{y} - \boldsymbol{F}(\boldsymbol{x})]^{\mathrm{T}} \mathbf{S}_{\epsilon}^{-1} [\boldsymbol{y} - \boldsymbol{F}(\boldsymbol{x})] + [\boldsymbol{x} - \boldsymbol{x}_a]^{\mathrm{T}} \mathbf{S}_a^{-1} [\boldsymbol{x} - \boldsymbol{x}_a], \tag{17}$$

where $\boldsymbol{x}_a$ is the apriori profile, $\mathbf{S}_a$ is the apriori error covariance matrix, and $\mathbf{S}_e$ is the measurement error covariance matrix. The atmospheric state with the highest probability $\hat{\boldsymbol{x}}$ is the one that minimizes the cost function, which is achieved by setting its gradient to zero:

$$\nabla_{\boldsymbol{x}} J(\hat{\boldsymbol{x}}) = 0. \tag{18}$$

The zero point is found by iteratively reducing the gradient using the Levenberg-Marquardt algorithm. For the analysis of the retrieval algorithm, standard retrieval metrics were used. The forward model Jacobian matrix $\mathbf{K}$ is defined as:

$$\mathbf{K}_{ij} = \frac{\partial \boldsymbol{F}_i}{\partial \boldsymbol{x}_j}. \tag{19}$$

It has units K$\mu$T$^{-1}$ and indicates how the spectrum at channel $i$ changes in response to variations of the state vector at altitude grid point $j$. Higher values of $\mathbf{K}$ mean higher sensitivity of the measured spectrum to the atmospheric state. The Jacobian of

https://doi.org/10.5194/egusphere-2026-2364
Preprint. Discussion started: 20 May 2026


the inverse model $\hat{\boldsymbol{x}} = \boldsymbol{F}^{-1}(\boldsymbol{y})$, which is also referred to as the contribution function or gain matrix $\mathbf{G}$, can be expressed in the symbolic form:

$$\mathbf{G}_{ij} = \frac{\partial \hat{\boldsymbol{x}}_i}{\partial \boldsymbol{y}_j}. \tag{20}$$

In contrast to the forward model Jacobian, the gain matrix has units of $\mu\mathrm{TK}^{-1}$ and indicates changes of the state vector at altitude grid point $i$ resulting from variations in the spectrum at channel $j$. The gain matrix is commonly used to calculate the observational error covariance matrix $\mathbf{S}_o$ by mapping the measurement covariance matrix $\mathbf{S}_\epsilon$ into the state space:

$$\mathbf{S}_o = \mathbf{G}\mathbf{S}_\epsilon\mathbf{G}^T. \tag{21}$$

The most used retrieval quantity is the Averaging kernel $\mathbf{A}$, defined as:

$$\mathbf{A} = \mathbf{G}\mathbf{K}. \tag{22}$$

For each altitude grid point $i$, the $i$-th row of the AVK matrix is a distribution function that represents the contribution of all grid points to the retrieved quantity $\hat{\boldsymbol{x}}_i$. The full width at half maximum (FWHM) of this function provides an estimate of the vertical resolution $\boldsymbol{dz}$ of the retrieval, and the weighted sum yields the measurement response $\boldsymbol{mr}$:

$$\boldsymbol{mr}_i = \frac{\mathbf{A}_i \boldsymbol{x}_a}{\boldsymbol{x}_{ai}}. \tag{23}$$

For altitude grid points where the measurement response $\boldsymbol{mr}$ is less than 0.6, the retrieved value cannot be trusted. By weighing the apriori covariance $\mathbf{S}_a$ with $\mathbf{A}$ we obtain the smoothing error $\mathbf{S}s$:

$$\mathbf{S}_s = (\mathbf{A} - \mathbf{I})\,\mathbf{S}_a\,(\mathbf{A} - \mathbf{I})^{\mathrm{T}}, \tag{24}$$

where $\mathbf{I}$ denotes the identity matrix. Another product of the AVK matrix that was used in the analysis is the Shannon information content $H$ defined as:

$$H = -\frac{1}{2}\det(\mathbf{I} - \mathbf{A}), \tag{25}$$

This quantity has units of bits and reflects the reduction in entropy after retrieving the atmospheric state. Specifically, it indicates that $2^H$ different atmospheric states can be distinguished by the retrieval algorithm. Unlike other measures, the Shannon information content is a scalar value, making it particularly suitable for direct comparisons between different retrieval algorithms.

## 3 Instrumentation

### 3.1 TEMPERA-C

TEMPERA-C is a ground-based microwave radiometer designed to measure the four Stokes components of the oxygen fine structure lines around 53 GHz with high spectral resolution (Tab. 1) (Krochin et al., 2022, 2026). The Stokes components are

https://doi.org/10.5194/egusphere-2026-2364
Preprint. Discussion started: 20 May 2026


measured using an Orthomode Transducer (OMT), which decomposes the incoming signal into two orthogonally polarized states. An on-board Field-Programmable Gate Array (FPGA) performs real-time Fast Fourier Transform (FFT) analysis on the two complex signals and accumulates the total power of each linear polarization, as well as the real and imaginary parts of the cross-correlated signals. The instrument is mounted on a fully rotatable platform that provides 360° azimuthal coverage. A secondary motor adjusts the elevation mirror between 0° and 90° while an additional linear motor compensates for standing waves through transverse translations of the mirror. To calibrate a fully polarimetric instrument, it is necessary to characterize the system's cross-polarization and phase shift. For operational calibration of our instrument, we have developed an automated calibration method. The innovation of our calibration approach lies in utilizing symmetry properties of the Zeeman-split spectra to estimate the phase shift. While the cross-polarization still needs to be measured in the laboratory, the phase shift can be continuously calibrated during operation. Instrument gain and offset are measured through a two-point calibration with an ambient load and built-in noise diodes. Both the front-end and back-end of the instrument are housed in a weatherproof enclosure and thermally stabilized with temperature-controlled ventilation. The temperature of the ambient load is monitored by three temperature sensors, alongside four sensors at the front-end and one at the back-end. Additionally, four temperature sensors positioned in the ventilation system measure the incoming and outgoing airflow.


**Figure 4.** TEMPERA-C at the Zimmerwald Observatory. The illustration was taken by a webcam installed on the platform on February 5, 2026.

### 3.2 Instrumental Setup

TEMPERA-C has been deployed at the Zimmerwald Observatory, part of the University of Bern in Switzerland, since January 2026. It conducts continuous routine measurements (Fig. 4) using three different observation directions (Tab. 1) and two positions of the linear motor. After each sky scan, a calibration sequence is performed by activating the noise diodes and rotating the internal mirror towards the ambient load. Each scan lasts for 3 seconds. The calibrated spectra are integrated during post-processing until a noise equivalent differential temperature (NEDT) of less than 0.15 K is achieved, which typically requires about 20 minutes of integration time for a single observation. An on-site weather station continuously measures surface pressure, temperature, and humidity, which are essential for modeling the retrieval algorithm. In the event of precipitation, a

https://doi.org/10.5194/egusphere-2026-2364
Preprint. Discussion started: 20 May 2026


built-in rain sensor notifies the system, prompting it to interrupt the measurement mode and move to a parking position to prevent moisture intrusion.

| Instrument specifications: | |
|---|---|
| Line center 1 | 53.066934 GHz |
| Line center 2 | 53.595775 GHz |
| Spectral width | 8×100 MHz |
| Channels | 8×4096 MHz |
| Channel width | 24.4 kHz |
| Integration time | 20 min |
| NEDT | $<$ 0.15 K |
| Instrument noise | 250 - 280 K |
| Polarization | $T_v, T_h, T_3, T_4$ |

| Platform specifications: | |
|---|---|
| Altitude | 900 m.a.s.l |
| Latitude | 46° 5'N |
| Longitude | 7° 3' E |
| Magnetic Inclination | 62.97° |
| Magnetic Declination | 3.3° |
| Magnetic field strength | 48152.2 nT |

| Observation geometry: | azimuth [°] | elevation [°] |
|---|---|---|
| LOS 1 | 0 | 60 |
| LOS 2 | - | 90 |
| LOS 3 | -120 | 45 |

**Table 1.** Instrument and experimental details of the TEMPERA-C deployment at the Zimmerwald observatory and main measurement sequence parameters.

### 3.3 GOES-19

The Geostationary Operational Environmental Satellite 19 (GOES-19) is part of the GOES-R series and was launched in 2024 by the National Oceanic and Atmospheric Administration (NOAA). The satellite operates in a geostationary orbit at an altitude of approximately 42000 km and a longitude of -75° E. One of its mission objectives is to enhance space weather monitoring and forecasting. The instruments used in this manuscript include the Magnetospheric Particle Sensor - High Energy (MPS-HI), the Extreme Ultraviolet and X-ray Irradiance Sensors (EXIS), and the Magnetometer (MAG). More detailed information can

https://doi.org/10.5194/egusphere-2026-2364
Preprint. Discussion started: 20 May 2026


be found in the data book (Vargas (2024)), as well as on the GOES website (https://www.goes-r.gov/) and the NOAA website (https://www.ncei.noaa.gov/). The dataset was accessed through the NOAA website (GOES-19 level 2 data (2026)).

## 4 Methodology

### 4.1 Model Setup for Synthetic Retrievals

To estimate the feasibility of magnetic field retrievals with TEMPERA-C and to determine the optimal measurement setup, the method of synthetic retrievals with simulated emission spectra was used. This approach involves the radiative transfer forward simulation of emission line spectra with a modified state vector $\boldsymbol{x_F}$, followed by an inversion where normally distributed noise is added. The perturbation of the state vector $\Delta\boldsymbol{x} = \boldsymbol{x_F} - \boldsymbol{x}_a$ was modeled with a Gaussian function that peaks at an altitude of 50 km, with a maximum value of 1 $\mu$T. Through this procedure, we optimized the algorithm for convergence, determined the a priori covariance matrix, and derived Jacobian, Gain, and AVK matrices for various observing geometries. The model atmosphere was set up on a latitude, longitude grid with a step size of 0.2° centered at the measurement location with the coordinates 46° 5' N and 7° 3' E. Temperature and humidity profiles were generated using a 4-year average of the WACCM-X model. This run was validated with radiometric ozone and water vapor measurements (Shi et al., 2025). The oxygen volume mixing ratio, which remains relatively constant up to an altitude of 80 km, was set at 20.9129%. The pressure grid was selected such that the resulting altitude grid has approximately 2 km spacing in the troposphere and 1 km above. Altitude grid coordinates were computed from the pressure, temperature, and humidity grid using hydrostatic equilibrium. The Radiative transfer calculations cover two oxygen emission lines centered at 53.066934 GHz and 53.595775 GHz with a bandwidth of 2×15 MHz, a spectral resolution of 24.4 kHz, and consider the Zeeman effect (Sec. 2.2), pressure broadening, Doppler broadening, as well as line mixing effects from the oxygen molecule. The impact of water vapour on the optical depth around 53 GHz was included by using the Rosenkranz continuum model (Rosenkranz (1998)). Otherwise, the radiative transfer calculations were performed under clear sky conditions. The normally distributed noise added to the simulated spectra had a standard deviation of 0.1 K. For the a priori state $\boldsymbol{x}_a$, we used the International Geomagnetic Reference Field (IGRF 13, Alken et al. (2021)), which is implemented in ARTS. The a priori covariance matrix $\mathbf{S}_a$ was chosen such that the a priori standard deviation $\boldsymbol{\sigma}_a$ is 3% of the a priori value $\boldsymbol{x}_a$. The diagonal elements of $\mathbf{S}_a$ are:

$$\mathrm{diag}(\mathbf{S}_a) = \boldsymbol{\sigma}_a^2, \boldsymbol{\sigma}_a = 0.03\boldsymbol{x}_a, \tag{26}$$

while the off-diagonal elements are calculated by:

$$\mathbf{S}_{a(ij)} = \boldsymbol{\sigma}_{a(i)}\boldsymbol{\sigma}_{a(j)} \exp\left(\frac{|z_i - z_j|}{z_c}\right). \tag{27}$$

The correlation length $z_c$ was set to 5 km. The Zeeman effect in the oxygen molecule exhibits a characteristic polarization pattern that strongly depends on the direction of observation (Sec. 2.2). Therefore, it is essential to determine the optimal LOS for each magnetic field component. To achieve this, simulations were performed multiple times with various sets of polarizations arranged over a grid of azimuth and elevation angles. This grid spans a full 360° cycle in azimuth and covers an

https://doi.org/10.5194/egusphere-2026-2364
Preprint. Discussion started: 20 May 2026


elevation range of 25° to 90° with a step size of 5°. Due to the high optical depth in the troposphere, retrieving stratospheric or mesospheric quantities at lower elevations in this spectral band is not feasible. The optimal LOS can be identified from this set of synthetic retrievals by comparing the Shannon information content $H$.

### 4.2 Model Setup for Measurement Retrievals

The retrieval algorithm used for inverting the measurements is based on the ideal case algorithm of synthetic retrievals, but includes several modifications. Observations from two different viewing directions were retrieved simultaneously using LOS 1 and LOS 2, as described in Table 1, along with the two circular polarizations $T_{lc}, T_{rc}$. The measurement error was increased from 0.1 K to 0.15 K, and the a priori error $\boldsymbol{\sigma}_a$ was raised from 3% to 4% of the a priori profile. To account for the variability in tropospheric optical depth, the tropospheric profiles of pressure, temperature, and humidity were modeled by linear interpolation, based on a priori profile values at 3 km altitude and surface measurements from the Zimmerwald observatory weather station. Also, a baseline retrieval was included, which retrieves the coefficients of a linear function in addition to the forward model spectrum. The atmospheric temperature was not part of the retrieval quantities in the synthetic case; its significant influence on the spectral line shape requires the inclusion of the temperature profile in the state vector for the measurement retrieval algorithm. The temperature a priori error was set to $\boldsymbol{\sigma}_a$ = 30 K.

### 4.3 Weather Monitoring

While lighter clouds have a minor impact on the frequency band at 53 GHz, heavy cloud coverage and precipitation significantly contribute to the tropospheric opacity. Therefore, periods of such conditions must be excluded from the dataset. The detection of rainfall and heavy clouds involves three different metrics and is part of the post-processing phase. Rainfall is detected using a built-in rain sensor and through an increase in surface relative humidity above 98% with a corresponding drop in surface temperature. The influence of cloud coverage is assessed by monitoring the brightness temperature of the line wings, which show a significant and sudden increase when heavy clouds enter the field of view. Additionally, the weather state is monitored by a webcam on the instrument platform, which captures an image every 5 minutes. Contaminated observations are flagged and can be ignored in further analyses.

## 5 Results

### 5.1 Simulation Results

The performance of the retrieval algorithm strongly depends on the line-of-sight (LOS) due to the polarization pattern of the Zeeman effect. To identify the optimal observation geometry, the Shannon information content $H$ was compared for various LOS configurations. Figure 5 illustrate $H$ as a function of the LOS for using two sets of polarization states: right and left circular polarization $(T_{lc}, T_{rc})$ and horizontal and vertical polarization $(T_v, T_h)$, respectively. The plots show regions where $H$ approaches zero, suggesting that retrievals of magnetic field components within these areas will not yield meaningful

https://doi.org/10.5194/egusphere-2026-2364
Preprint. Discussion started: 20 May 2026


results. On the contrary, regions with relatively high $H$ values are theoretically well-suited for retrieving the corresponding magnetic field components. The figures also highlight which components of the magnetic field $\boldsymbol{H} = (\boldsymbol{H_u}, \boldsymbol{H_v}, \boldsymbol{H_w})$ can potentially be retrieved. For instance, the retrievals of $\boldsymbol{H_u}$ components consistently result in $H$ values below 0.01 across all LOS configurations and both sets of polarization, indicating a low likelihood of successful retrieval. However, the retrievals for $\boldsymbol{H_w}$ components using the circularly polarized setup achieve a maximum $H$ value of 6.8, suggesting a much higher chance to retrieve the physical state from measurements. Additionally, the analysis reveals that for an LOS near azimuth = 180° and elevation = 60° which is nearly parallel to the magnetic field lines, $H$ remains close to zero. The locations of the maximal $H$ values are summarized in Tab. 2. The following discussion focuses solely on results corresponding to the LOS with the highest $H$ values. Synthetic retrievals using two circularly polarized spectra $T_{lc}, T_{rc}$ have an effective altitude range where $\boldsymbol{mr}(z) > 0.6$ for the retrieved $\boldsymbol{H}_w$ component, between 30-75 km. The effective altitude range for the $\boldsymbol{H}_v$ component is somewhat smaller, between 35-60 km. The retrieved profiles $\hat{\boldsymbol{x}}$ show convergence towards the forward model profiles $\boldsymbol{x}_F$ in these ranges (Fig. 6). The vertical resolution $\boldsymbol{dz}$ is 9-10 km in the stratosphere and 10-16 km in the mesosphere for $\boldsymbol{H}_w$, while for $\boldsymbol{H}_v$ it ranges between 9-13 km and 13-19 km, respectively. The retrievals of the $\boldsymbol{H}_u$ component have almost diminishing measurement response and show no tendency to match the forward model profile, which is consistent with the near-zero Shannon information content $H$. Similar results were observed for retrievals conducted with linearly polarized spectra $T_v, T_h$, but with a smaller effective altitude range, higher vertical resolution, lower Jacobian values, and reduced information content. Retrievals using a full rank Stokes vector $T_I, T_Q, T_U, T_V$ performed slightly better than those using linearly polarized spectra, but showed no improvement compared to the retrievals with circularly polarized spectra. Since these simulations are of no relevance for our analysis, the results of the full Stokes retrievals can be found in Appendix C.

### 5.2 Stokes Spectra Observations

Before entering the continuous measurement mode described in Section 3.2, we conducted measurements for various observation geometries. An example of measured $T_Q$, $T_U$, and $T_V$ for azimuths of az = 0°, 90°, 180° is shown in Fig. 7. The elevation angle for these observations is constant at 60° because comparisons at different elevations are challenging due to varying air mass in the field of view. For comparison with simulations, the polarization frame was rotated to match that of ARTS (Sec. 2.1). The measured spectra show that $T_V$, which represents the circularly polarized $\sigma^{\pm}$ components, has a maximal magnitude at an azimuth of 180°, which is nearly parallel to the magnetic field lines. A minimum is observed at an azimuth of 0°, where the angle between the observation direction and the magnetic field lines is approximately 60°. Measurements taken at an elevation of 30°, which is nearly perpendicular to the field lines, are shown in Fig. B1. For an observation direction that is perpendicular to the magnetic field lines, the $T_V$ signal is expected to vanish. This is reflected in Fig. B1, where the observed $T_V$ parameter is nearly zero in magnitude. However, due to a slight deviation from an exact perpendicular view, a small signal remains visible. Additionally, because of the curvature of the geomagnetic field lines, each observation direction from our latitudes will always contain both parallel and perpendicular components. The $T_Q$ parameters show their highest magnitude at an azimuth of 0° and are almost zero at an azimuth of 90°. In contrast, $T_U$ parameters are highest at an azimuth of 90° and lowest at an azimuth of 0°. Both parameters drop to zero at an azimuth of 180° since the signal from the relatively weak perpendicular component is

https://doi.org/10.5194/egusphere-2026-2364
Preprint. Discussion started: 20 May 2026


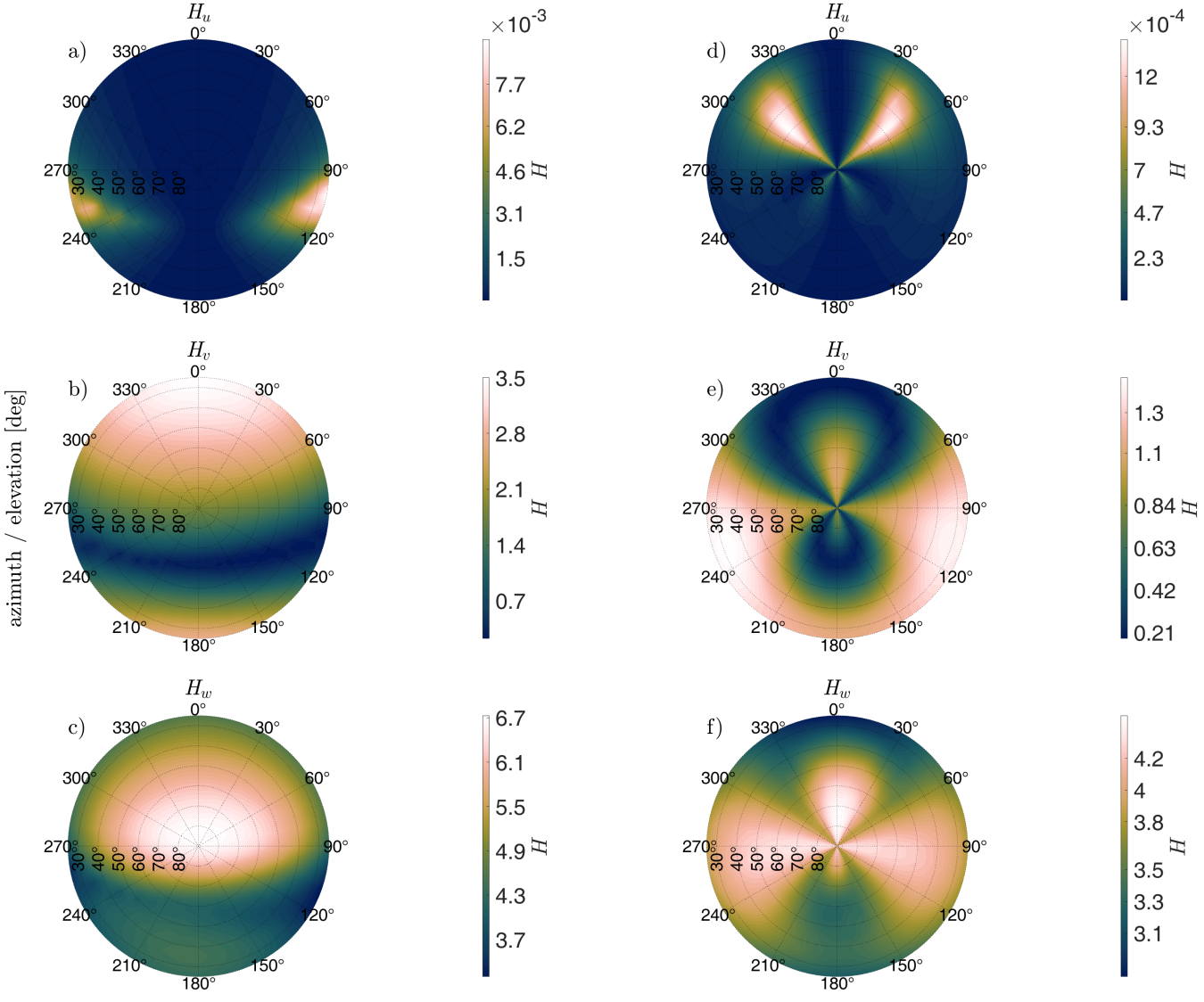


**Figure 5.** The Shannon information content $H$ (Eq. 25) is calculated for the retrieval algorithm using two circularly polarized spectra $T_{lc}$ and $T_{rc}$ (a - c), as well as for the two linearly polarized spectra $T_v, T_h$ (d - f). The information content is shown for each component of $\boldsymbol{H} = (\boldsymbol{H}_u, \boldsymbol{H}_v, \boldsymbol{H}_w)$. The azimuth angle for the corresponding simulation is represented by the angular coordinate, while the elevation is represented by the radial coordinate.

insufficient to show a contribution, and are therefore not shown in the figure. Both the $\pi$ and $\sigma^{\pm}$ components can be seen in the plots of $T_Q, T_U$ at LOS's for which they remain detectable.

https://doi.org/10.5194/egusphere-2026-2364
Preprint. Discussion started: 20 May 2026


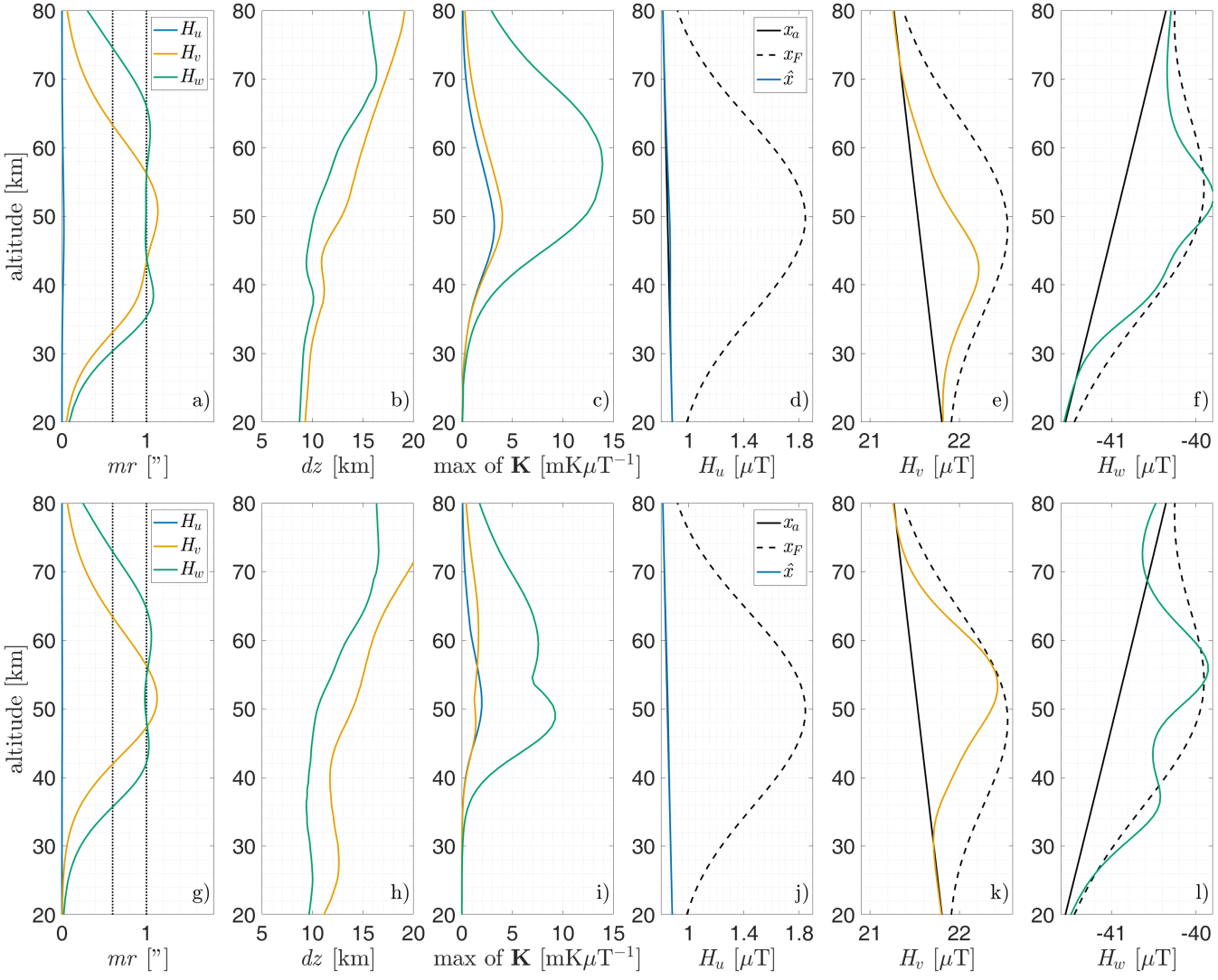


**Figure 6.** Results of the retrieval algorithm with two circularly polarized spectra $T_{lc}, T_{rc}$ (a - f), as well as for the two linearly polarized spectra $T_v, T_h$ (g - l). a, g) Measurement response $\boldsymbol{mr}$; b, h) vertical resolution $\boldsymbol{dz}$; c, i) spectral maximum of the forward model Jacobian $\mathbf{K}$; d - f, j - l) Retrieved state $\hat{\boldsymbol{x}}$ in comparison to the apriori state $\boldsymbol{x_a}$ and the forward model state $\boldsymbol{x_F}$. Retrievals of individual field components $\boldsymbol{H} = (\boldsymbol{H}_u, \boldsymbol{H}_v, \boldsymbol{H}_w)$ were performed with different LOS, which can be found in Tab. 2.

### 5.3 Results From Measurement Retrievals

From the set of retrieved field components $\boldsymbol{H}_u, \boldsymbol{H}_v, \boldsymbol{H}_w$, only the vertical component $\boldsymbol{H}_w$ has values with $\boldsymbol{mr} > 0.6$. Compared to synthetic retrievals, the altitude range and vertical resolution are reduced (Fig. 8). The retrieved profiles show oscillations that appear to be a response to measurement noise. However, the magnetic field perturbations $d\boldsymbol{H} = \boldsymbol{H} - \text{mean}(\boldsymbol{H})$ seem to show a variability that can be related to a space weather event. On January 18, 2026, an X1.9 class solar flare was

https://doi.org/10.5194/egusphere-2026-2364
Preprint. Discussion started: 20 May 2026


| $T_{lc}, T_{rc}$ | $H_{max}$ | az [deg] | el [deg] |
|---|---|---|---|
| $\boldsymbol{H}_u$ | 0.01 | 260 | 25 |
| $\boldsymbol{H}_v$ | 3.57 | 0 | 25 |
| $\boldsymbol{H}_w$ | 6.80 | 0 | 85 |
| $T_v, T_h$ | | | |
| $\boldsymbol{H}_u$ | $15{\cdot}10^{-3}$ | 50 | 60 |
| $\boldsymbol{H}_v$ | 1.51 | 110 | 30 |
| $\boldsymbol{H}_w$ | 4.51 | 0 | 75 |
| $T_I, T_Q, T_U, T_V$ | | | |
| $\boldsymbol{H}_u$ | $59{\cdot}10^{-3}$ | 260 | 25 |
| $\boldsymbol{H}_v$ | 2.86 | 0 | 25 |
| $\boldsymbol{H}_w$ | 5.69 | 10 | 5 |

**Table 2.** Summary of maximal retrieved Shannon information content $H_{max}$ for defined viewing geometries for different polarimetric quantities such as left and right circular polarized radiation $T_{lc}, T_{rc}$, horizontal and vertical polarization $T_v, T_h$, and the four Stokes components $T_I, T_Q, T_U, T_V$.

observed at 18:19 UTC, which triggered a strong geomagnetic storm that affected even middle latitudes. Several aurora sightings were reported across Europe, including Switzerland. During this time, the TEMPERA-C instrument continuously measured under stable weather conditions. The time series of $d\boldsymbol{H}_w$ calculated from the retrieved profiles of $\boldsymbol{H}_w$, along with an average over the altitude range of 40-60 km, is illustrated in Fig. 9. Observations contaminated by weather influence have been blanked. The data shows a perturbation lasting approximately 5 days, with a magnitude of $d\boldsymbol{H}_{w,max} = -130$ nT during the geomagnetic storm. The total retrieval error was estimated to be about 3 $\mu$T, resulting from both measurement and a priori covariance. When this error is treated as normally distributed noise, the peak value error is calculated to be $\Delta(d\boldsymbol{H}_{w,max}) = 180$ nT. This high value can be explained by the high value of the a priori error, which is 4% of the a priori profile and has absolute values of about 1.64 $\mu$T. Throughout the time series, the standard deviation on a single altitude grid point does not exceed 78 nT. For the average over the effective altitude range, the standard deviation resulted in 62 nT. For comparison with our measurements, we chose proton flux measurements from MPS-HI, X-ray flux measurements from EXIS, and in situ magnetic field data from the MAG instrument on the GOES-19 satellite. The dataset was binned on the same time grid, which has a temporal resolution of 1 hour. The satellite data indicate the arrival of both X-ray and proton flux shortly after the solar flare, and the geomagnetic disturbance is evident between January 19 and 23.

https://doi.org/10.5194/egusphere-2026-2364
Preprint. Discussion started: 20 May 2026


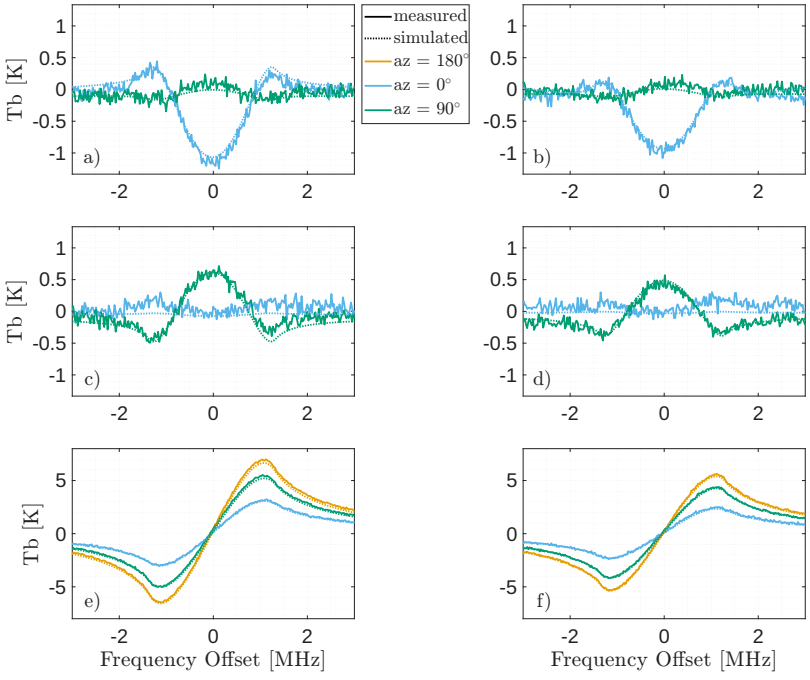


**Figure 7.** Spectra measured by TEMPERA-C at the Zimmerwald Observatory for an elevation of 60° across different azimuth angles along with the corresponding ARTS simulations:
a, b) $T_Q$ Stokes parameter; c, d) $T_U$ Stokes parameter; e, f) $T_V$ Stokes parameter; a - e) line center at 53.066934 GHz; b - f) line center at 53.595775 GHz;

## 6 Discussion

The observations of the $T_Q, T_U$, and $T_V$ parameters reflect the polarization pattern discussed in Sec. 2.2. The $\pi$ components, which are polarized perpendicularly to the magnetic field lines, exhibit the highest values in the $T_Q$ Stokes parameter, particularly at an azimuth of 0°. This configuration results in nearly perpendicular geometry between the line of sight (LOS) and the magnetic field, where the field lines are aligned with the vertical polarization axis. In contrast, when the azimuth is at 90°, the magnetic field lines are tilted by approximately 60° relative to the polarization frame, leading to a dominant contribution to the $T_U$ parameter. The $T_V$ parameters reach their highest values when viewed along the magnetic field lines, while they are almost zero when viewed nearly perpendicular to them. Simulation offsets are attributed to several factors. The temperature profile of the model atmosphere differs from the actual physical state, which accounts for the differences in magnitude. Additionally, the magnetic field model used in ARTS contains small deviations from the real conditions where the orientation of the field lines can deviate by up to 0.5°with a magnitude of a few hundred nT. Secondly, measurement offsets contribute to the overall discrepancy. Residual standing waves may introduce an offset of up to 0.1 K. The instrument's pointing offset has an inaccuracy of 0.2° which could contribute to an additional offset. Furthermore, residual cross-polarization effects can contribute an offset up to 0.1 K. Calculating radiative transfer in the troposphere within this frequency band presents challenges

https://doi.org/10.5194/egusphere-2026-2364
Preprint. Discussion started: 20 May 2026


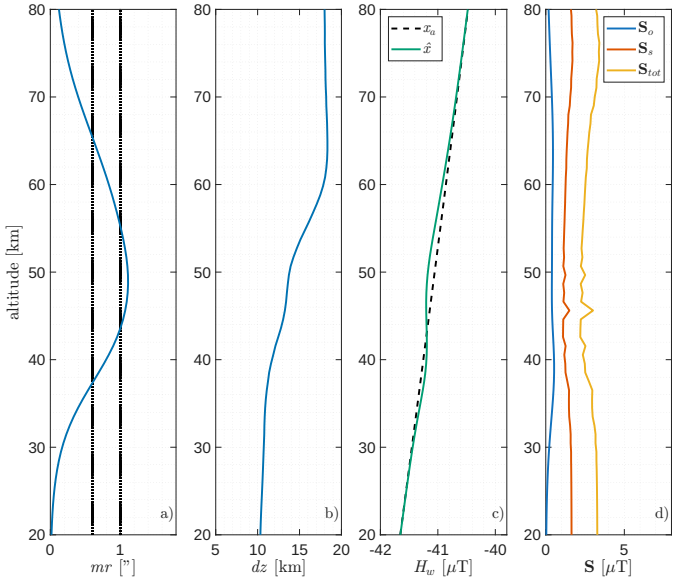


**Figure 8.** Results of the retrieval algorithm with two circularly polarized spectra $T_{lc}, T_{rc}$ observed by TEMPERA-C:
a) Measurement response $\boldsymbol{mr}$; b) vertical resolution $\boldsymbol{dz}$; c) Retrieved state $\hat{\boldsymbol{x}}$ in comparison to the apriori state $\boldsymbol{x}_a$; d) Retrieval error (Eq. 21, 24), where $\mathbf{S}_{tot} = \mathbf{S}_o + \mathbf{S}_s$.

due to several factors. In addition to pressure broadening, the line mixing effect must also be considered. Furthermore, water vapor significantly impacts optical depth. As a result, correcting for the tropospheric contribution represents a large portion of the overall error. Finally, it is important to consider potential errors in the calculation of the Zeeman effect algorithm for these relatively sensitive signals. A discussion of the observed Stokes parameters across various observation geometries, a detailed analysis of the various error contributions, and the offsets compared to ARTS simulations is planned for a subsequent publication. For this manuscript, a comprehensive quantification of all possible contributions is beyond the scope, as the focus is on retrieval algorithms with circularly polarized spectra.

The synthetic retrieval results demonstrate the capability to retrieve the $\boldsymbol{H}_w$ component of the magnetic field and a smaller, yet still significant potential to retrieve $\boldsymbol{H}_v$ within the presented setup. The simulations also show that high sensitivity is required for the observation setup. A NEDT of 0.1 K is, in general, a very low value for ground-based radiometry. The maximal Shannon information content of $H = 6.8$, even though sufficient for carefully performed retrievals, also highlights the necessity for very high measurement sensitivity. In comparison, retrievals of atmospheric temperature with the same setup yield Shannon information values of approximately $H = 20$. The potential for retrieving $\boldsymbol{H}_u$ components was found to be nearly nonexistent, primarily due to the relatively low magnitude of this component. The $\boldsymbol{H}_u$ component is about 50 times weaker than the $\boldsymbol{H}_w$ component, which also affects the a priori error that scales linearly with the a priori profile $\boldsymbol{x}_a$. For the same reason, the performance of the $\boldsymbol{H}_v$ retrieval is slightly less effective than that of the $\boldsymbol{H}_w$ retrieval. Moreover, the simulations showed

https://doi.org/10.5194/egusphere-2026-2364
Preprint. Discussion started: 20 May 2026


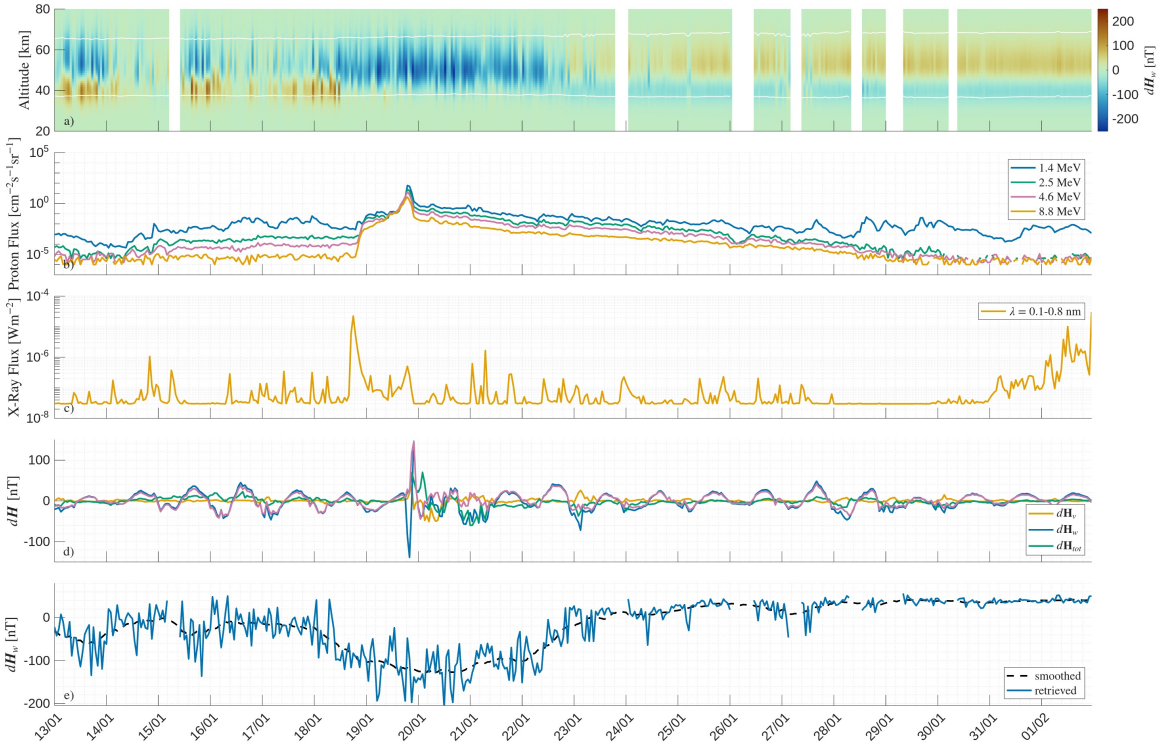


**Figure 9.** Result from retrievals with TEMPERA-C observations along with GOES-19 data for comparison:
a) series of retrieved $d\boldsymbol{H}_w$ profiles with the $\boldsymbol{mr} = 0.6$ levels illustrated by white lines. b) GOES MPS-HI Proton flux; c) GOES EXIS long wave X-Ray flux; d) GOES MAG magnetic field perturbation; e) $d\boldsymbol{H}_w$ average over 40-60 km. Smoothing was performed using a running mean with a window length of 20 hours.

higher performance when using the two circular polarizations for the retrievals compared to using two linear polarizations. Interestingly, the usage of the full rank Stokes did not show additional advantage.

The retrieval based on actual measurements has lower performance than the one based on synthetic retrievals. This is expected, as the instrument's NEDT is higher than that used in the synthetic retrieval algorithm. Calibration inaccuracy and small spectral artefacts, which are part of the measurement error, can further influence retrieval outcomes, given the high sensitivity requirements. In addition, the ideal case does not account for atmospheric variability, and the tropospheric state is known exactly in this context. In contrast, the retrieval algorithm utilizing actual observations operates under uncertainty regarding the state of the troposphere and the tropospheric optical depth. In our algorithm, we model tropospheric profiles using surface measurements, which is the best option available, but it inevitably introduces model uncertainty, increasing the overall error

https://doi.org/10.5194/egusphere-2026-2364
Preprint. Discussion started: 20 May 2026


budget. Furthermore, an additional potential issue regarding the retrieval of $\boldsymbol{H}_v$ is that the observations were performed at a higher elevation than the optimum of el = 35° suggested by Fig. 5. However, achieving such a low elevation angle proves challenging due to the contributions of tropospheric error. In practice, obstacles within the field of view and the contribution from side lobes can become problematic at very low elevation angles.

Currently, the retrieved magnetic field profiles primarily reflect the sensitivity of the model rather than the actual physical state. However, both the measurement response and vertical resolution are on a high level, demonstrating the general feasibility of retrieving the vertical magnetic field component $\boldsymbol{H}_w$ using the presented method. The perturbation of the vertical magnetic field component $d\boldsymbol{H}_w$ corresponds to the geomagnetic storm, with a maximum magnitude of $d\boldsymbol{H}_{w,max} = -130$ nT, which falls within a typical range for such events. The recovery phase, following the peak of the event, can last for several days (Kamide and Chian (2007)). Estimating the start time of the initial phase of the peak poses some challenges for several reasons. First, the noise level of $d\boldsymbol{H}_w$ is relatively high compared to the weak signal and slow changes. An analysis of the standard deviation of the vertical average (see Fig. 9, Panel e) shows $\sigma = 62$ nT, leading to a signal-to-noise ratio of $\frac{d\boldsymbol{H}_{w,max}}{\sigma} = 2.1$. While this ratio is adequate for detecting the maximum peak and its value, it is insufficient for accurately determining the exact start and end times. Additionally, earlier solar flares may influence the observed magnetic field perturbations. A Kp value over 5 and aurora forecasts were reported between January 16th and 17th. Consequently, residual artifacts from earlier geomagnetic activity cannot be disregarded. Assessing the specific impact on observations at our latitudes is complex and beyond the scope of this manuscript.

The comparison with GOES-19 observations indicates that the start time of the retrieved geomagnetic perturbation aligns with the sudden increase in proton and X-ray flux. Although the increase in the retrieved perturbation appears to begin slightly earlier, this discrepancy can be explained by several factors mentioned earlier. The proton flux gradually decreases, which corresponds to the recovery phase of the geomagnetic field perturbation. Protons penetrate deeper into the atmosphere and can reach the mesosphere and even stratopause, potentially triggering perturbations in the geomagnetic field. X-rays are often absorbed by ionizing oxygen and nitrogen atoms in the thermosphere (Turunen et al. (2009)). The magnitude of the vertical geomagnetic field perturbation observed by GOES-19 closely matches our retrieved results, falling within the established error budget. However, the initial and recovery phases are not evident in these observations. It is important to note that the altitude of the GOES-19 satellite, at 42000 km, is significantly higher than that of our measurements, so we would not expect to see the same distinction in the three phases.

## 7 Conclusions

The synthetic retrievals show the feasibility of retrieving the $\boldsymbol{H}_v$ and $\boldsymbol{H}_w$ in the altitude range between 35-60 km and 30-75 km, respectively, with an altitude resolution between 10-15 km. Simulations for a set of different viewing directions highlight the importance of carefully selecting the observation geometry to achieve optimal retrieval results. Circularly polarized spectra

https://doi.org/10.5194/egusphere-2026-2364
Preprint. Discussion started: 20 May 2026


appear to provide more information content compared to linearly polarized ones, while including additional Stokes parameters in the measurement vector showed no improvement. The retrieval results from actual observations reveal the challenges associated with measurements and a finite knowledge of the atmospheric physical state. Currently, the quality of retrievals and associated errors remains at an experimental level. However, a geomagnetic storm has been detected within a reasonable magnitude of the magnetic $\boldsymbol{H}_w$ component deviation. This demonstrates the sensitivity of the measurement setup to perturbations in the geomagnetic field. It is important to note that TEMPERA-C was initially designed for retrieving atmospheric temperatures and is not optimized for the application discussed in this manuscript. An instrument specifically built for monitoring the geomagnetic field should be optimized for the frequency band and spectral resolution. To enhance tropospheric corrections, incorporating broadband channels that measure the slope of the left wing of the 60 GHz oxygen band could be advantageous. With a more accurate tropospheric correction, retrievals could be improved by observing at lower elevations. Additionally, deployment at higher altitudes would enhance retrieval performance by reducing the influence of the troposphere. The most critical factor is achieving a low NEDT, ideally in the range of 0.05 K or lower. This could be accomplished by cooling the front end of the instrument. Currently, the TEMPERA-C front end is thermally stabilized at a temperature of 298 K but is not actively cooled. The desired noise level could be reached through cryogenic cooling of the instrument's front end, as for example in Filinis et al. (2025), where an NEDT of 0.04 K was achieved.

https://doi.org/10.5194/egusphere-2026-2364
Preprint. Discussion started: 20 May 2026


## Appendix A: Landé factors and relative line strength

The representation of the Landé factor $g$ used in Fig. 3 is from Lenoir (1968):

$$g = g_s \frac{J(J+1) + S(S+1) - N(N+1)}{2J(J+1)}, \tag{A1}$$

with a molecule-dependent factor $gs = 2.002064$ (Christensen and Veseth (1978)), that takes into account relativistic corrections and the spin-angular momentum coupling of the electron. While the Landé factors derived from this equation are sufficient for illustrative purposes, the Zeeman model implemented in ARTS considers higher-order Zeeman corrections and mixing between the individual fine structure levels (Larsson et al. (2019)). The relative line strength $S_{M,M'}$ for transitions with $\Delta J = -1$ can be found in Schadee (1978):

$$S^{\pi}_{M,M'} = \frac{3\left(J^2 - M^2\right)}{2J(2J-1)(2J+1)} \tag{A2}$$

$$S^{\sigma^{\pm}}_{M,M'} = \frac{3(J \mp M)(J-1 \mp M)}{4J(2J-1)(2J+1)} \tag{A3}$$

(A4)

## Appendix B: Additional Stokes Spectra Observations

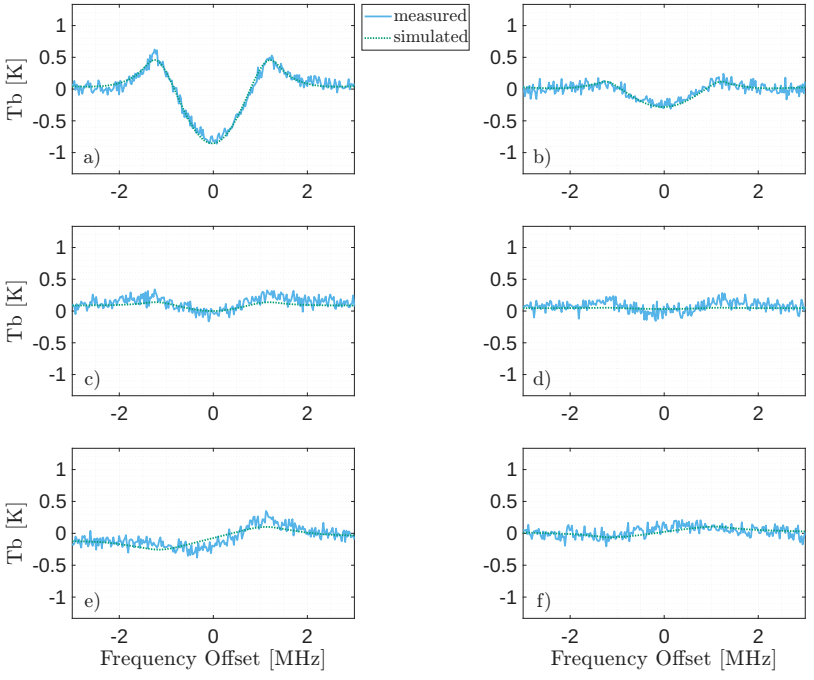


**Figure B1.** Same as Fig. 7 for an azimuth angle of 0° and an elevation of 30° .

https://doi.org/10.5194/egusphere-2026-2364
Preprint. Discussion started: 20 May 2026


## Appendix C: Results of Full Stokes Retrievals

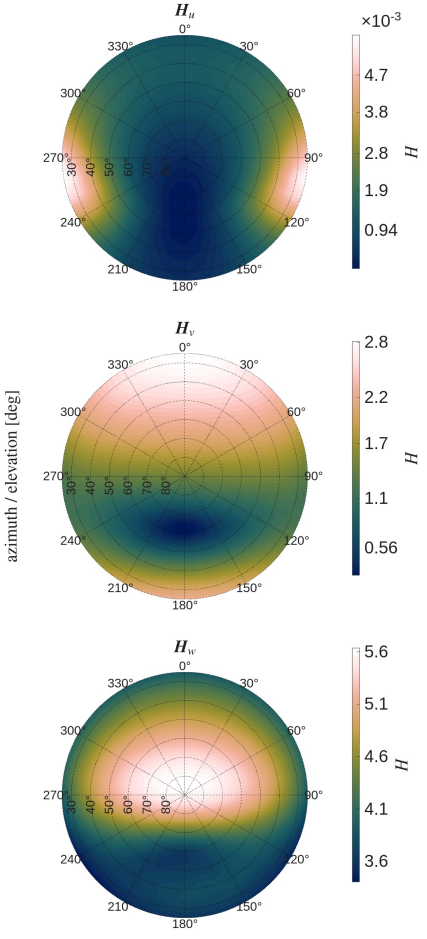


**Figure C1.** Same as Fig. 5 but for the retrieval algorithm with a full rank Stokes vector $T_I, T_Q, T_U, T_V$,.

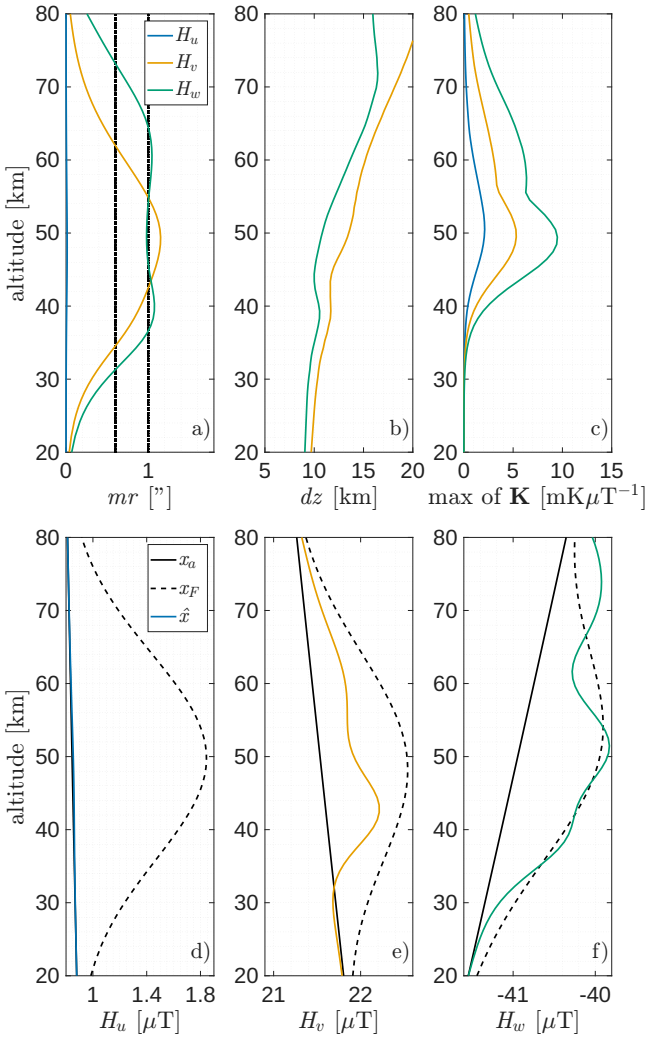


**Figure C2.** Same as Fig. 6, but for the retrieval algorithm with a full rank Stokes vector $T_I, T_Q, T_U, T_V$,.

https://doi.org/10.5194/egusphere-2026-2364
Preprint. Discussion started: 20 May 2026


*Author contributions.* WK developed the calibration scheme, performed the calibration, implemented the retrieval, and the data analysis of TEMPERA-C observations. WK and GS conceptualized the content of the manuscript. AM guided and supported the preparation of the paper. All authors contributed to the editing of the manuscript.

*Competing interests.* Gunter Stober declares that he is a member of the editorial board of Annales Geophysicae.

*Data availability.* The TEMPERA-C Level 1 and Level 2 data can be shared upon request (witali.krochin@unibe.ch)

*Acknowledgments.* This research has been supported by the Schweizerischer Nationalfonds zur Förderung der Wissenschaftlichen Forschung (grant no. 200021L-228107), and the Swiss Polar Institute (SPI) supports the development of the TEMPERA-C radiometer. We thank the ARTS developer team for their support and Richard Larsson for implementing the Zeeman and Line-Mixing effect in ARTS. Scientific color maps (Crameri et al., 2020) are used in this study to prevent visual distortion of the data and exclusion of readers with color-vision deficiencies.

https://doi.org/10.5194/egusphere-2026-2364
Preprint. Discussion started: 20 May 2026


## References

Alken, P., Thébault, E., Beggan, C. D., Amit, H., Aubert, J., Baerenzung, J., Bondar, T. N., Brown, W. J., Califf, S., Chambodut, A., Chulliat, A., Cox, G. A., Finlay, C. C., Fournier, A., Gillet, N., Grayver, A., Hammer, M. D., Holschneider, M., Huder, L., Hulot, G. G., Jager, T., Kloss, C., Korte, M., Kuang, W., Kuvshinov, A., Langlais, B., Léger, J.-M., Lesur, V., Livermore, P. W., Lowes, F. J., Macmillan, S., Magnes, W., Mandea, M., Marsal, S., Matzka, J., Metman, M. C., Minami, T., Morschhauser, A., Mound, J. E., Nair, M., Nakano, S., Olsen, N., Pavón-Carrasco, F. J., Petrov, V. G., Ropp, G., Rother, M., Sabaka, T. J., Sanchez, S., Saturnino, D., Schnepf, N. R., Shen, X., Stolle, C., Tangborn, A., Tøffner-Clausen, L., Toh, H., Torta, J. M., Varner, J., Vervelidou, F., Vigneron, P., Wardinski, I., Wicht, J., Woods, A., Yang, Y., Zeren, Z., and Zhou, B.: International geomagnetic reference field: the thirteenth generation, Earth Planets and Space, 73, 49, https://doi.org/10.1186/s40623-020-01288-x, 2021.

Angelopoulos, V.: The THEMIS mission, Space Sci Rev, 141, https://doi.org/10.1007/s11214-008-9336-1, 2008.

Buehler, S. A., Eriksson, P., Kuhn, T., von Engeln, A., and Verdes, C.: ARTS, the Atmospheric Radiative Transfer Simulator, Journal of Quantitative Spectroscopy and Radiative Transfer, 91(1), 65–93, https://doi.org/10.1016/j.jqsrt.2004.05.051, 2005.

Buehler, S. A., Mendrok, J., Eriksson, P., Perrin, A., Larsson, R., and Lemke, O.: ARTS, the Atmospheric Radiative Transfer Simulator – version 2.2, the planetary toolbox edition, Geoscientific Model Developement, 11, 1537–1556, https://doi.org/10.5194/gmd-11-1537-2018, 2018.

Buehler, S. A., Larsson, R., Lemke, O., Pfreundschuh, S., Brath, M., Adams, I., S. Fox, F. R., Czarnecki, P., and Eriksson, P.: The Atmospheric Radiative Transfer Simulator ARTS, Version 2.6 — Deep Python Integration, Journal of Quantitative Spectroscopy and Radiative Transfer, Preprint, https://doi.org/10.2139/ssrn.4815661, 2024.

Christensen, H. and Veseth, L.: On the high-precision Zeeman effect in O2 and SO, Journal of Molecular Spectroscopy, 72, 438–444, https://doi.org/10.1016/0022-2852(78)90142-X, 1978.

Crameri, F., Shephard, G. E., and Heron, P.: The misuse of colour in science communication, Nature Communications, 11, https://doi.org/10.1038/s41467-020-19160-7, 2020.

Eriksson, P., Buehler, S. A., Kuhn, T., von Engeln, A., and Verdes, C.: ARTS, the atmospheric radiative transfer simulator, Version 2, Journal of Quantitative Spectroscopy and Radiative Transfer, 112, 1551–1558, https://doi.org/10.1016/j.jqsrt.2011.03.001, 2011.

Escoubet, C. P., Fehringer, M., and Goldstein, M.: Introduction: The Cluster mission, Annales Geophysicae, 19, 1197–1200, https://doi.org/10.5194/angeo-19-1197-2001, 2001.

Filinis, A., Bell, A., Murk, A., and Stober, G.: Development of a new cryogenically cooled water vapor radiometer for the 22 GHz line – quasi-optical design and preliminary laboratory receiver tests, EGUsphere, 2025, 1–25, https://doi.org/10.5194/egusphere-2025-5664, 2025.

Friis-Christensen, E., Lühr, H., Knudsen, D., and Haagmans, R.: Swarm – An Earth Observation Mission investigating Geospace, Advances in Space Research, 41, 210–216, https://doi.org/10.1016/j.asr.2006.10.008, 2008.

Gautier, D.: INFLUENCE OF TERRESTIAL MAGNETIC FIELD ON MILLIMETRIC WAVES IN MOLECULAR OXYGEN IN ATMOSPHERE, ANNALES DE GEOPHYSIQUE, 23, 535+, 1967.

GOES-19 level 2 data: National Oceanic and Atmospheric Administration (NOAA), https://data.ngdc.noaa.gov/platforms/solar-space-observing-satellites/goes/goes19/l2/data/, 2026.

https://doi.org/10.5194/egusphere-2026-2364
Preprint. Discussion started: 20 May 2026


Johansson, R., Raffalski, U., Milz, M., and Larsson, R.: Microwave radiometric measurements and simulations of the Zeeman-affected rotational transition of oxygen at 233.95 GHz, Journal of Quantitative Spectroscopy and Radiative Transfer, 346, 109 579, https://doi.org/10.1016/j.jqsrt.2025.109579, 2025.

Kamide, Y. and Chian, A.: Handbook of the Solar-Terrestrial Environment, Springer, https://doi.org/10.1007/978-3-540-46315-3, 2007.

Krochin, W., Stober, G., and Murk, A.: Development of a Polarimetric 50-GHz Spectrometer for Temperature Sounding in the Middle Atmosphere, IEEE Journal of selected topics in applied earth observations and remote sensing, 15, https://doi.org/10.48350/186172, 2022.

Krochin, W., Murk, A., Luder, A., and Stober, G.: Operational calibration of a ground-based fully polarimetric radiometer for stratospheric temperature retrievals, Atmospheric Measurement Techniques, 19, 2103–2123, https://doi.org/10.5194/amt-19-2103-2026, 2026.

Larsson, R., Ramstad, R., Mendrok, J., Buehler, S. A., and Kasai, Y.: A method for remote sensing of weak planetary magnetic fields: Simulated application to Mars, Geophysical Research Letters, 40, 5014–5018, https://doi.org/10.1002/grl.50964, 2013.

Larsson, R., Buehler, S. A., Eriksson, P., and Mendrok, J.: A treatment of the Zeeman effect using Stokes formalism and its implementation in the Atmospheric Radiative Transfer Simulator (ARTS), Journal of Quantitative Spectroscopy and Radiative Transfer, 133, 445–453, https://doi.org/10.1016/j.jqsrt.2013.09.006, 2014.

Larsson, R., Lankhaar, B., and Eriksson, P.: Updated Zeeman effect splitting coefficients for molekular oxygen in planetary applications, Geoscientific Model Developement, 224, 431–438, https://doi.org/10.1016/j.jqsrt.2018.12.004, 2019.

Lenoir, W. B.: Propagation of Partially Polarized Waves in a Slightly Anisotropic Medium, Journal of Applied Physics, 38, 5283–5290, https://doi.org/10.1063/1.1709315, 1967.

Lenoir, W. B.: Microwave spectrum of molecular oxygen in the mesosphere, Journal of Geophysical Research, 73, 361–376, https://doi.org/10.1029/JA073i001p00361, 1968.

Liebe, H. J.: Modeling attenuation and phase of radio waves in air at frequencies below 1000 GHz, Radio Science, 16, 1183–1199, https://doi.org/10.1029/RS016i006p01183, 1981.

Mishchenko, M., Travis, L., and Lacis, A.: Scattering, Absorption, and Emission of Light by Small Particles, Cambridge University Press, https://books.google.ch/books?id=i6r1YFyK_g8C, 2002.

Misra, S., Padmanabhan, S., Kangaslahti, P., Montes, O., Bosch-Lluis, J., Cofield, R., and Ramos, I.: The Electrojet Zeeman Imaging Explorer (EZIE) mission and the Microwave Electrojet Magnetogram (MEM) radiometer instrument, in: Small Satellite Conference, 3, https://doi.org/10.26077/8pny-k893, 2022.

Misra, S., Padmanabhan, S., Kangaslahti, P., Cofield, R., Montes, O., Perez, I. R., Dergevorkian, A., Scott White, R., Cooperrider, J. T., Lim, H., Javadi, H., Bosch-Lluis, X., Wang, M., Pradhan, O., Gasiewski, A. J., and Yee, J.-H.: Spectral Calibration of the Microwave Electrojet Magnetogram Radiometer Instrument on the Electrojet Zeeman Imaging Explorer Mission, IEEE Transactions on Geoscience and Remote Sensing, 63, 1–10, https://doi.org/10.1109/TGRS.2025.3625889, 2025.

Neubert, T., Mandea, M., Hulot, G., von Frese, R., Primdahl, F., Jørgensen, J. L., Friis-Christensen, E., Stauning, P., Olsen, N., and Risbo, T.: Ørsted satellite captures high-precision geomagnetic field data, Eos, Transactions American Geophysical Union, 82, 81–88, https://doi.org/https://doi.org/10.1029/01EO00043, 2001.

Padmanabhan, S., Misra, S., Kangaslahti, P., Montes, O., Bosch-Luis, J., Cofield, R., Ramos, I., and Yee, S.: Microwave Electrojet Magnetogram (MEM) Instrument for the Electrojet Zeeman Imaging Explorer (EZIE) Mission, in: IGARSS 2022 - 2022 IEEE International Geoscience and Remote Sensing Symposium, pp. 7337–7340, https://doi.org/10.1109/IGARSS46834.2022.9884004, 2022.

https://doi.org/10.5194/egusphere-2026-2364
Preprint. Discussion started: 20 May 2026


Pardo, J., Pagani, L., Gerin, M., and Prigent, C.: Evidence of the zeeman splitting in the 21 ⟶ 01 rotational transition of the atmospheric 16O18O molecule from ground-based measurements, Journal of Quantitative Spectroscopy and Radiative Transfer, 54, 931–943, https://doi.org/https://doi.org/10.1016/0022-4073(95)00129-9, 1995.

Randa, J., Lahtinen, J., Camps, A., Gasiewski, A., Hallikainen, M., Leine, D., Martin-Neira, M., Piepmeier, J., Rosenkranz, P., Ruf, C., Shiue, J., and Skou, N.: Recommended Terminology For Microwave Radiometry, https://tsapps.nist.gov/publication/get_pdf.cfm?pub_id=33079, 2008.

Reigber, C., Schwintzer, P., and Lühr, H.: The CHAMP geopotential mission, Bulletin of Theoretical and Applied Geophysics, 40, 285–289, https://bgo.ogs.it/sites/default/files/2023-08/bgta40.3.4_REIGBER1.pdf, 1999.

Rodgers, C. D.: Inverse Methods for Atmospheric sounding Theory and Practice, World Scientific, https://doi.org/doi.org/10.1142/3171, 2000.

Rosenkranz, P. W.: Water vapor microwave continuum absorption: A comparison of measurements and models, Radio Science, 33, 919–928, https://doi.org/10.1029/98RS01182, 1998.

Rosenkranz, P. W. and Staelin, D. H.: Polarized thermal microwave emission from oxygen in the mesosphere, Radio Science, 23, 721–729, https://doi.org/https://doi.org/10.1029/RS023i005p00721, 1988.

Schadee, A.: On the Zeeman effect in electronic transitions of diatomic molecules, Journal of Quantitative Spectroscopy and Radiative Transfer, 19, 517–531, https://doi.org/10.1016/0022-4073(78)90020-1, 1978.

Schwartz, M., Read, W., and Van Snyder, W.: EOS MLS forward model polarized radiative transfer for Zeeman-split oxygen lines, IEEE Transactions on Geoscience and Remote Sensing, 44, 1182–1191, https://doi.org/10.1109/TGRS.2005.862267, 2006.

Shi, G., Liu, H., Tsutsumi, M., Gulbrandsen, N., Kozlovsky, A., Pokhotelov, D., Lester, M., Jacobi, C., Wu, K., and Stober, G.: New insights into the polar ozone and water vapor, radiative effects, and their connection to the tides in the mesosphere–lower thermosphere during major sudden stratospheric warming events, Atmospheric Chemistry and Physics, 25, 9403–9430, https://doi.org/10.5194/acp-25-9403-2025, 2025.

Turunen, E., Verronen, P. T., Seppälä, A., Rodger, C. J., Clilverd, M. A., Tamminen, J., Enell, C.-F., and Ulich, T.: Impact of different energies of precipitating particles on NOx generation in the middle and upper atmosphere during geomagnetic storms, Journal of Atmospheric and Solar-Terrestrial Physics, 71, 1176–1189, https://doi.org/https://doi.org/10.1016/j.jastp.2008.07.005, high Speed Solar Wind Streams and Geospace Interactions, 2009.

Vargas, D.: Geostationary Operational Environmental Satellite – R Series (GOES-U), GOES-U Data Book, Lockheed Martin Space, https://www.goes-r.gov/downloads/resources/documents/GOES-U%20DataBook.pdf, 2024.

Waters, J., Froidevaux, L., Harwood, R., Jarnot, R., Pickett, H., Read, W., Siegel, P., Cofield, R., Filipiak, M., Flower, D., Holden, J., Lau, G., Livesey, N., Manney, G., Pumphrey, H., Santee, M., Wu, D., Cuddy, D., Lay, R., Loo, M., Perun, V., Schwartz, M., Stek, P., Thurstans, R., Boyles, M., Chandra, K., Chavez, M., Chen, G.-S., Chudasama, B., Dodge, R., Fuller, R., Girard, M., Jiang, J., Jiang, Y., Knosp, B., LaBelle, R., Lam, J., Lee, K., Miller, D., Oswald, J., Patel, N., Pukala, D., Quintero, O., Scaff, D., Van Snyder, W., Tope, M., Wagner, P., and Walch, M.: The Earth observing system microwave limb sounder (EOS MLS) on the aura Satellite, IEEE Transactions on Geoscience and Remote Sensing, 44, 1075–1092, https://doi.org/10.1109/TGRS.2006.873771, 2006.

Yee, J. H., Gjerloev, J., Wu, D., and Schwartz, M. J.: First Application of the Zeeman Technique to Remotely Measure Auroral Electrojet Intensity From Space, Geophysical Research Letters, 44, 10,134–10,139, https://doi.org/10.1002/2017GL074909, 2017.

Yee, J.-H., Gjerloev, J., and Wu, D.: Remote Sensing of Magnetic Fields Induced by Electrojets From Space, chap. 21, pp. 451–468, American Geophysical Union (AGU), https://doi.org/10.1002/9781119815631.ch21, 2021.